Advances in Industrial and Manufacturing Engineering 7 (2023) 100127

Contents lists available at ScienceDirect

Advances in Industrial and Manufacturing Engineering

journal homepage: www.sciencedirect.com/journal/advances-in-industrial-and-manufacturing-engineering

A software for research and education in ductile damage

R.F.V. Sampaio [a], N.S.M. Alexandre [a], J.P.M. Pragana [a], I.M.F. Bragança [a,b], C.M.A. Silva [a], P.A.F. Martins [a,*]

[a] IDMEC, Instituto Superior Técnico, Universidade de Lisboa, Portugal
[b] CIMOSM, Instituto Superior de Engenharia de Lisboa, Instituto Politécnico de Lisboa, Portugal

ARTICLE INFO

Keywords:
Metal forming
Ductile fracture
Experimentation
Software
Education

ABSTRACT

This paper gives insight into the development and utilization of a computer software that uses raw experimental data from the load cells and DIC systems to obtain the instant of time at fracture t_f, the loading paths in principal strain space $\varepsilon_1 = f(\varepsilon_2)$, and their conversion into the space of effective strain vs. stress triaxiality $\bar{\varepsilon} = f(\eta)$. Special emphasis is given to the different assumptions and stress triaxiality measures that can be used to convert the loading paths from principal strain space into the space of effective strain vs. stress triaxiality. Results for double-action radial extrusion show the differences of treating the loading paths as linear or non-linear from beginning until the onset of failure by fracture. Results also allow concluding on the importance of accounting for the stress triaxiality derived from individual experimental measurements in an average sense over the entire loading paths, to avoid overestimation and mislocation of the fracture forming limits. The applicability of the software for education and training of students in formability is also discussed.

1. Introduction

Formability refers to the ability of a material to undergo plastic deformation without failure. In the case of sheet metal forming, formability is generally associated with the amount of strain to which a material can be deformed without the occurrence of plastic instability (i.e., necking) or fracture. Therefore, its quantification is essential to prevent defects and to ensure the fabrication of sound sheet metal parts.

Pioneering investigations on the formability of sheets were conducted by Keeler (1965) and Goodwin (1968). The first of these researchers (Keeler, 1965), introduced the circle grid analysis technique (CGA) by imprinting a grid of circles on a sheet surface before stamping in order to determine the in-plane principal strains, plot their evolution $\varepsilon_1 = f(\varepsilon_2)$ in the tension-tension quadrant of principal strain space, and compare their values against the critical strains for which defects were observed. The second of these researchers (Goodwin, 1968), utilized the same methodology to determine and plot the first in-plane strain evolution (i.e., strain loading path) in the tension-compression quadrant of principal strain space.

Ever since its proposal more than five decades ago, principal strain space has been widely used to plot the strain loading paths resulting from sheet metal forming processes and the material formability limits due to plastic instability (the so-called forming limit curve - FLC) (Paul, 2021) and fracture (the so-called fracture forming limits – FFL's) (Isik et al., 2014).

In the case of bulk metal forming, circle grid analysis and principal strain space were first utilized by Kuhn et al. (1973). Failure in bulk forming, in contrast to sheet forming, is mainly caused by fracture (Martins et al., 2014), despite necking being possible to occur in regions of the parts encompassing three-dimensional to plane stress material flow transitions, as it was recently shown by Sampaio et al. (2023a). Differences between the three-dimensional stress conditions of bulk forming and the plane stress conditions of sheet forming are often employed to distinguish the circumstances under which cracks initiate and propagate in both types of processes. In fact, as recently shown by Martins et al. (2014), the fracture forming limits of sheet forming are due to crack opening by tension (mode I of fracture mechanics) or by in-plane shearing (mode II), whereas the fracture forming limits of bulk forming are due to crack opening by tension (mode I) or by out-of-plane shearing (i.e., through-thickness, mode III).

The space of effective strain vs. stress triaxiality $\bar{\varepsilon} = f(\eta)$ that was introduced by Hancock and Mackenzie (1976) is an alternative graphical environment for plotting the loading paths and material formability limits. It has two main advantages over principal strain space that justify

---

* Corresponding author.
E-mail addresses: rui.f.sampaio@tecnico.ulisboa.pt (R.F.V. Sampaio), n.alexandre@outlook.pt (N.S.M. Alexandre), joao.pragana@tecnico.ulisboa.pt (J.P.M. Pragana), ibraganca@dem.isel.ipl.pt (I.M.F. Bragança), carlos.alves.silva@tecnico.ulisboa.pt (C.M.A. Silva), pmartins@tecnico.ulisboa.pt (P.A.F. Martins).

https://doi.org/10.1016/j.aime.2023.100127
Received 3 July 2023; Received in revised form 18 August 2023; Accepted 18 August 2023
Available online 19 August 2023

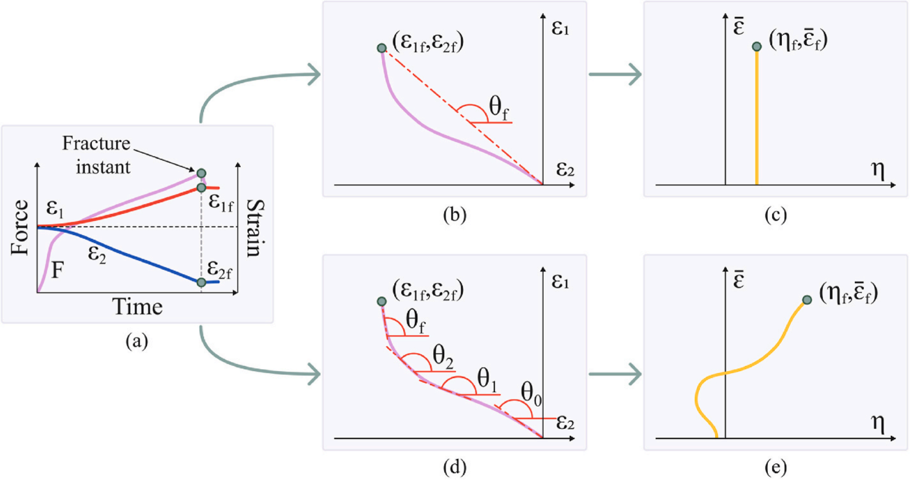

Fig. 1. Methodology for plotting the experimental results obtained from (a) force vs. time and in-plane strain vs. time evolutions in (b, d) principal strain space and (c, e) in the effective strain vs. stress triaxiality space assuming (b, c) linear and (d, e) non-linear loading paths.

its preferential use in the analysis of failure in bulk forming. Firstly, it can represent various loading paths instead of being limited to plane stress loading conditions. Secondly, it provides a better link with the states of stress acting in the parts due to the use of stress triaxiality $\eta = \sigma_m/\overline{\sigma}$, where σ_m is the hydrostatic stress and $\overline{\sigma}$ is the effective stress.

In the past two decades there has been an effort to add a third axis to the space of effective strain vs. stress triaxiality in order to include the dependency on the Lode's (1926) stress parameter $\mu = (\sigma_2 - \sigma_c)/\,\tau_{max}$, where $\sigma_c = (\sigma_1 + \sigma_3)/2$, $\tau_{max} = (\sigma_1 - \sigma_3)/2$ and $\sigma_1, \sigma_2, \sigma_3$ are the major, intermediate and minor principal stresses. However, the scope of application of this extended space $\overline{\varepsilon} = f(\eta, \mu)$ is limited because three-dimensional states of stress in bulk forming are generally associated with high negative stress triaxiality values under which fracture seldom occurs. In fact, because the formability test specimens that are commonly used to calibrate damage or fracture criteria in bulk forming generally fail by cracking under plane stress conditions, due to the necessity of having visible free surfaces to perform surface strain analysis, the associated Lode parameters can be easily expressed through a direct dependency on stress triaxiality (Bai and Wierzbicki, 2008). This means that calibration of critical damage or fracture criteria in bulk forming is currently done without an explicit dependency on the Lode parameter.

Still, the implicit presence of the Lode parameter in damage or fracture criteria must be emphasized due to its connection with shearing effects within the plastically deformed materials (Sampaio et al., 2022).

A major disadvantage on the utilization of the stress triaxiality space $\overline{\varepsilon} = f(\eta)$ results from the difficulty of transforming complex loading paths from principal strain space into a graphical environment built upon effective strain and stress triaxiality values. In fact, while most strain loading paths of sheet formability test specimens can be assumed as linear proportional, the same does not apply for the bulk formability test specimens, even though the assumption is often used by some researchers. This is because stress triaxiality η is pointwise dependent on the inverse slope of the strain loading path $\beta = d\varepsilon_2/d\varepsilon_1$, as follows (Martins et al., 2014),

$$\eta = \frac{\sigma_m}{\overline{\sigma}} = \frac{\sqrt{1+2r}(1+\beta)}{3\sqrt{1+\frac{2r}{1+r}\beta+\beta^2}} \tag{1}$$

The above equation applies to plane stress conditions along the free surfaces of the test specimens and r is the normal anisotropy according to Hill's (1948) yield criterion.

Fig. 1 illustrates the differences obtained when transforming a general strain loading path from principal strain space into the effective strain vs. stress triaxiality space under the assumption of linear (Fig. 1b and c) or non-linear (Fig. 1d and e) evolutions.

Determination of the in-plane strain evolutions (Fig. 1a) by circle grid analysis (CGA) implicates multiple measurements of the imprinted surface circles at pre-defined amounts of deformation. This is time-consuming and error prone and is nowadays replaced by digital image correlation (DIC), which is an optical photogrammetry technique that tracks the changes of an applied surface pattern by analyzing the images of the specimens during deformation (Peters and Ranson, 1982).

DIC is now established as the preferred technique to determine the formability limits by necking and fracture in sheet forming but its use in bulk forming is more recent and dates from only five years ago (Magrinho et al., 2018). In the case of bulk metal forming, and taking into consideration that the force-time evolution $F(t)$ in Fig. 1a is obtained from the load cell and the in-plane strain-time evolutions $\varepsilon_1(t)$, $\varepsilon_2(t)$ are obtained from DIC, the strain loading paths $\varepsilon_1 = f(\varepsilon_2)$ of Fig. 1b,d are constructed by combining the in-plane strain vs. time evolutions and removing the time dependency. The instant of fracture corresponds to the time t_f at which a sudden drop in force is observed.

So, in the case of assuming a linear evolution between the initial and final in-plane strain values (i.e., $\beta = d\varepsilon_2/d\varepsilon_1 \approx \varepsilon_{2f}/\varepsilon_{1f}$), the transformation of the experimental strain loading path from principal strain space into effective strain vs. stress triaxiality space is that shown in Fig. 1b and c. But, in the case of considering the non-linear evolution, transformation must account for the instantaneous slopes $\theta = f(\beta)$ along the strain loading paths,

$$\beta = \frac{d\varepsilon_2}{d\varepsilon_1} = \frac{1}{\tan\theta} \tag{2}$$

This is illustrated in Fig. 1d and e and is a much more accurate way to obtain the experimental evolution of stress triaxiality in the case of non-linear strain loading paths. The procedure was recently employed by the authors (Silva et al., 2023) to determine the stress triaxiality values at fracture.

Under these circumstances, this paper has a twofold objective. Firstly, to introduce new measures of stress triaxiality that account for the differences in the accumulation of damage between different stress states. Secondly, to present a software for processing raw experimental data from the load cell and DIC system to determine the instant of time at fracture t_f, the loading paths in principal strain space $\varepsilon_1 = f(\varepsilon_2)$, and their conversion into the space of effective strain vs. stress triaxiality $\overline{\varepsilon} = f(\eta)$ for arbitrary, non-linear, loading paths.

Results confirm the applicability of the software for handling and treating experimental data for scientific research purposes, and for educating and training students and technicians in different topics of material formability.

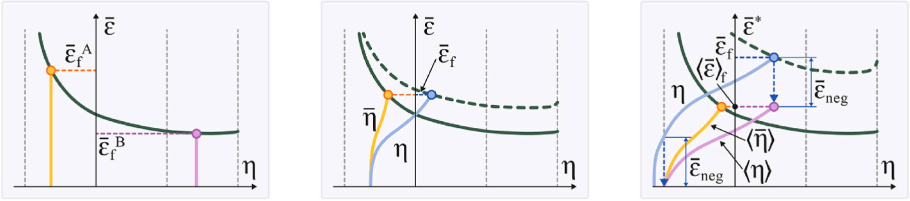

(a) (b) (c)

Fig. 2. Calibration of the fracture forming limit by means of (a) linear loading paths and (b) non-linear loading paths built upon instantaneous (blue curve) or weighted average (orange curve) stress triaxiality measures. The influence of high negative stress triaxiality values (blue curve) is shown in (c). (For interpretation of the references to colour in this figure legend, the reader is referred to the Web version of this article.)

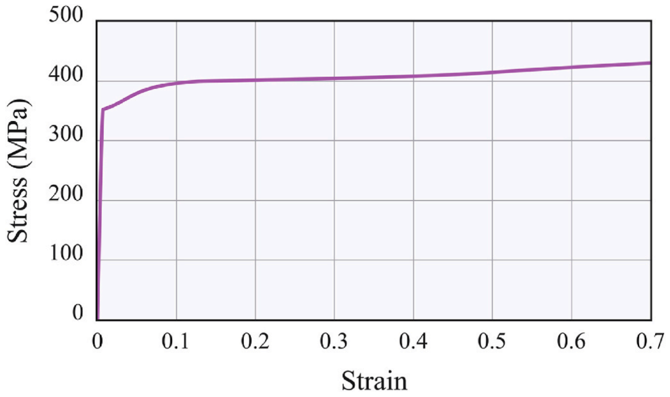

Fig. 3. Flow curve of the AA6082-T6 aluminum alloy.

2. Strategies for the evaluation of stress triaxiality

The problem of evaluating the forming limits of complex, non-linear, loading paths has been around for almost as long as there have been studies on the formability of sheet materials for automotive stamped parts (Ishigaki, 1978). In fact, although finite element digital twins can nowadays be used to calibrate damage and fracture criteria, the problem persists when experimental procedures are solely used to determine the material formability limits.

In general terms, one may claim that the conjugate pairs $(\eta_f, \bar{\varepsilon}_f)$ of stress triaxiality and effective strain at fracture are sufficient to calibrate the fracture forming limits when loading paths are linear up to fracture. This is shown in Fig. 2a where arbitrary linear paths up to fracture are utilized to obtain the fracture forming limit with a critical damage D_{crit} (refer to the dark green curve).

Additional conjugate pairs $(\eta_i, \bar{\varepsilon}_i)$ are needed in the case of non-linear loading paths because damage accumulates at different rates for different stress states. This is illustrated in Fig. 2b, in which a comparison between the use of instantaneous η_i and weighted average $\bar{\eta}$ stress triaxiality measures is provided. The latter is based on the numerical work of Suntaxi et al. (2021) in single point incremental forming of tubes, and is now defined for the piecewise treatment of experimental non-linear loading paths, as follows,

$$\bar{\eta} = \frac{\sum_{i=0}^{N} (\eta_i \Delta\bar{\varepsilon}_i)}{\bar{\varepsilon}} \tag{3}$$

In the above equation, N is the total number of measurements performed by the DIC system, $\Delta\bar{\varepsilon}_i$ is the increment of effective strain between measurements and $\bar{\varepsilon}$ is the total effective strain calculated from the in-plane strain values $(\varepsilon_1, \varepsilon_2)$ obtained from the DIC system. For this reason, the effective strain at fracture $\bar{\varepsilon}_f$ is independent from the instantaneous η_f and weighted average $\bar{\eta}_f$ stress triaxiality values at fracture.

The use of $\bar{\eta}$ is preferred to η_i because it accounts for the more significant stress states during plastic deformation. In mathematical terms, equation (3) can be seen as a weak form of equation (1) in which the instantaneous values of stress triaxiality η_i resulting from every experimental measurement i are accounted only in an average sense over the entire loading path. For this reason, $\bar{\eta}$ is likely to provide a closer link with the physics of damage accumulation and, therefore, a better compatibility between the effective strain at fracture $\bar{\varepsilon}_f$ and the fracture forming limit, depicted as the dark green curve corresponding to a critical value of damage D_{crit} (Fig. 2b).

Under these circumstances the dark green dashed curve in Fig. 2b may be seen as an ill-calibrated fracture forming limit due to the use of instantaneous values of stress triaxiality η_i.

Fig. 2c refers to the weighted average stress triaxiality at which damage accumulates $\langle\bar{\eta}\rangle$. This alternative stress triaxiality measure is determined by neglecting data in which instantaneous stress triaxiality values η_i are below a threshold η_{asym}, corresponding to the vertical asymptote of the ductile fracture criteria for which damage is not accumulated,

$$\langle\bar{\eta}\rangle = \frac{\sum_{i=0}^{N} \left(\eta_i \Delta\bar{\varepsilon}_i \frac{\langle \eta_i - \eta_{\mathrm{asym}} \rangle}{\eta_i - \eta_{\mathrm{asym}}} \right)}{\bar{\varepsilon}} \tag{4}$$

In the above expression, ⟨ ⟩ are Macaulay brackets and $\langle\bar{\eta}\rangle$ is the weighted average stress triaxiality at which damage accumulates (i.e., whenever $\eta_i > \eta_{\mathrm{asym}}$).

The utilization of equation (4) requires the definition of a new type of conjugate pair $(\langle\bar{\eta}\rangle, \langle\bar{\varepsilon}\rangle)$ to plot the loading path up to the fracture limit (refer to the orange curve in Fig. 2c), in which $\langle\bar{\varepsilon}\rangle$ refers to the amount of effective strain where damage accumulates,

$$\langle\bar{\varepsilon}\rangle = \sum_{i=0}^{N} \left(\Delta\bar{\varepsilon}_i \frac{\langle \eta_i - \eta_{\mathrm{asym}} \rangle}{\eta_i - \eta_{\mathrm{asym}}} \right) = \bar{\varepsilon} - \bar{\varepsilon}_{\mathrm{neg}} \tag{5}$$

In the above equation, the symbol $\bar{\varepsilon}_{\mathrm{neg}}$ corresponds to the amount of effective strain resulting from plastic deformation at high negative triaxiality stress states, in which there is no accumulation of damage. This is illustrated by the differences in the effective strain values of the blue and purple curves of Fig. 2c.

Under these circumstances, the vertical axis in Fig. 2c contains both the total effective strain $\bar{\varepsilon}$ values (i.e., the values used to plot the blue curve) and the effective strain values at which damage accumulates $\langle\bar{\varepsilon}\rangle$ (refer to the orange curve). The dark green dashed curve in Fig. 2c is once again a graphical representation of an ill-calibrated fracture limit resulting from the use of wrong conjugate pairs of stress triaxiality and effective strain at fracture.

3. Methods and procedures

3.1. Experimental and numerical analysis

The methodologies for transforming the strain loading paths from principal strain space into the effective strain vs. stress triaxiality space based on the concepts of weighted average stress triaxiality $\bar{\eta}$ and

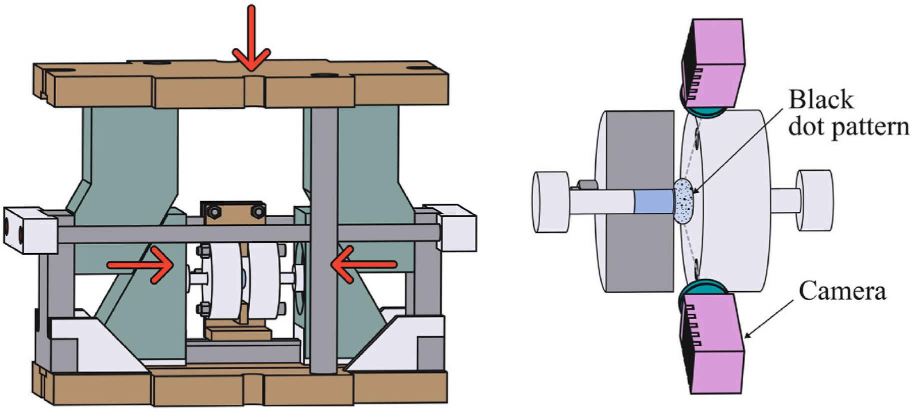

Fig. 4. Schematic representation of the experimental setup utilized in the double-action radial extrusion test with a detail of the DIC measuring conditions.

weighted average stress triaxiality at which damage accumulates $\langle\overline{\eta}\rangle$ were validated by means of experimental data on double-action radial extrusion retrieved from a previous publication of the authors (Sampaio et al., 2023a).

The experiments were performed on a medium-strength aluminum-magnesium-silicon alloy AA6082 in the solution heat-treated (T6) state and the flow curve of the material at ambient temperature was determined by means of compressions tests carried out on cylindrical test specimens with a 20 mm diameter and a 20 mm height (Fig. 3).

Fig. 4 provides a schematic illustration of the experimental setup utilized in the double-action radial extrusion experiments. The evolution of the extrusion force with time $F(t)$ was taken from a load cell installed in the hydraulic testing machine (Instron SATEC 1200 kN) where the experiments were performed, and the evolution of the in-plane principal strains with time $(\varepsilon_1, \varepsilon_2) = f(t)$ on the outer surface of the test specimens was obtained from a DIC system (model Q-400 3D from Dantec Dynamics).

The DIC system was equipped with two 6-megapixels resolution cameras with 50.2 focal lenses and f/8 aperture at an angle of 40–60° and the measuring regions of the specimens were painted in white and subsequently sprayed with a black speckle pattern. An acquisition frequency (shutter frequency) of 10Hz was used.

After getting the experimental force-time evolutions $F(t)$ from the load cell and the in-plane strain-time evolutions $(\varepsilon_1, \varepsilon_2) = f(t)$ from the DIC system, the instant of fracture t_f, the strain loading paths in principal strain space $\varepsilon_1 = f(\varepsilon_2)$, and their transformation into effective strain vs. stress triaxiality space $\overline{\varepsilon} = f(\eta)$, were determined by using a software built upon the previously described stress triaxiality measures. The next section provides details of the software from a developer and user's perspective.

3.2. *Software development, user flow, and interface*

The software was developed using the.NET MAUI (Microsoft, 2023) cross-platform framework with the programming languages C# for the functional elements and XAML for the user interface (UI).

Fig. 5 presents a simplified version of the user flow where the numbers inside brackets refer to the equations included in the paper. The utilization of weighted average stress triaxiality measures $\overline{\eta}$ and weighted average stress triaxiality measures at which damage accumulates $\langle\overline{\eta}\rangle$ to convert the loading paths from principal strain space to effective strain vs. stress triaxiality space involves numerical implementation of equations (1)–(5).

The software user flow of Fig. 5 requires implementation of the pseudo code shown below, in which appropriate reference to the equations previously introduced are included in brackets.

Fig. 6 provides screenshots of the two software user interfaces: (i) the 'Analyzer' and (ii) the 'Calibrator' for an example consisting of a rod tension test. The 'Analyzer' interface (Fig. 6a) allows uploading the files containing raw experimental data from the load cell containing the force–time evolutions and from the DIC system containing the strain–time evolutions to determine the instants of necking and fracture (if, existent) and the corresponding loading paths in principal strain space and in the effective strain vs. stress triaxiality space. As seen, the strain loading path in principal strain space is close to the theoretical estimate in pure tension ($\beta = -1/2$) and the transformation into the strain vs. stress triaxiality space replicates the theoretical value of $\eta = 1/3$ more closely in the case of using weighted average stress triaxiality measures $\overline{\eta}$ instead of instantaneous ones.

Conversion of the experimental in-plane strain-time evolutions $(\varepsilon_1, \varepsilon_2) = f(t)$ obtained from DIC into principal strain space is carried out in two different stages. Firstly, the raw experimental data is filtered to eliminate noise by means of a symmetric moving average filter (Smith, 2003),

$$y_i = \frac{1}{2M+1}\left(\sum_{j=1}^{M} x_{i-j} + x_i + \sum_{j=1}^{M} x_{i+j}\right) \tag{6}$$

where $2M+1$ is the number of data points used in the average (i.e., the window size), x is the input raw data and y is the output filtered data.

Secondly, the step interval n_{slope} selected by the user is employed to calculate the inverse slope $\beta = d\varepsilon_2/d\varepsilon_1$ of the strain loading path (Fig. 7) that will be used in the conversion into the space of effective strain vs. stress triaxiality by means of equation (1),

$$\beta = \frac{1}{\tan\theta} = \frac{d\varepsilon_2}{d\varepsilon_1} \approx \frac{\Delta\varepsilon_2}{\Delta\varepsilon_1} = \frac{(\varepsilon_2)_i - (\varepsilon_2)_{i-n_{\text{slope}}}}{(\varepsilon_1)_i - (\varepsilon_1)_{i-n_{\text{slope}}}} \tag{7}$$

So, in the case of $n_{\text{slope}} = N$ the strain loading paths are treated as linear, whereas in the case of $n_{\text{slope}} < N$ the changes in β are accounted to match the non-linear characteristics of the loading paths.

Other features provided by the 'Analyzer' comprise the possibility of tuning the inverse slope of the strain loading path $\beta = d\varepsilon_2/d\varepsilon_1$ at the instant of fracture, and of allowing the first n_{slope} points being proportional or non-proportional, in which case the slope is calculated with reference to the origin at every step up to n_{slope}.

The 'Calibrator' interface (Fig. 6b) makes use of the effective strain vs. stress triaxiality space and of the loading paths calculated by the 'Analyzer' to calibrate multiple ductile fracture criteria such as: normalized Cockcroft-Latham (after Cockcroft and Latham, 1968; due to Oh et al., 1979), McClintock (after McClintock, 1968, due to Ayada et al., 1987), maximum shear (Martins et al., 2014), Rice and Tracey (1969), Oyane (1972), Tai and Yang (1987), Lou et al. (2012), Isik (2018), and Sampaio et al. (2023b).

Once a criterion is selected, its main parameters such as, for example, the critical damage D_{crit} at crack opening, can be supplied to adjust the

```
SET Count to n_step
FOR each instant in PrincipalStrains123
    IF Count is equal to n_step THEN
        CALCULATE PrincipalStrains123Increments with Count and 0
        CALCULATE EffectiveStrainIncrement
        CALCULATE Beta (equation 2)
        CALCULATE StressTriaxiality (equation 1)
        CALCULATE AverageStressTriaxiality (equation 3)
        IF StressTriaxiality is greater than Asymptote THEN
            CALCULATE EffectiveStrainAtWhichDamageAccumulates (equation 5)
            MAKE StressTriaxialityAtWhichDamageAccumulates equal to StressTriaxiality
            CALCULATE AverageStressTriaxialityAtWhichDamageAccumulates (equation 4)
        END IF
        SET InitialCount to 0
        WHILE InitialCount is less than n_step
            IF ProportionalCheckBox is checked THEN
                MAKE EffectiveStrainIncrement at InitialCount equal to StrainIncrements at
                n_step
                MAKE StressTriaxiality at InitialCount equal to StressTriaxiality at n_step
                MAKE AverageStressTriaxiality at InitialCount equal to
                AverageStressTriaxiality at n_step
                IF StressTriaxiality is greater than Asymptote THEN
                    MAKE EffectiveStrainAtWhichDamageAccumulates at InitialCount equal to
                    EffectiveStrainAtWhichDamageAccumulates at n_step
                    MAKE StressTriaxialityAtWhichDamageAccumulates at InitialCount equal to
                    StressTriaxialityAtWhichDamageAccumulates at n_step
                    MAKE AverageStressTriaxialityAtWhichDamageAccumulates at InitialCount
                    equal to AverageStressTriaxialityAtWhichDamageAccumulates at n_step
                END IF
            END IF
            INCREMENT InitialCount
        END WHILE
    ELSE
        CALCULATE PrincipalStrains123Increments with Count and (Count - n_step)
        CALCULATE EffectiveStrainIncrement
        CALCULATE Beta (equation 2)
        CALCULATE StressTriaxiality (equation 1)
        CALCULATE AverageStressTriaxiality (equation 3)
        IF StressTriaxiality is greater than Asymptote THEN
                CALCULATE EffectiveStrainAtWhichDamageAccumulates (equation 5)
                MAKE StressTriaxialityAtWhichDamageAccumulates equal to StressTriaxiality
                CALCULATE AverageStressTriaxialityAtWhichDamageAccumulates (equation 4)
        END IF
    END IF
    INCREMENT Count
END FOR
```

Pseudo code of the software.

fracture forming limit to the loading paths up to fracture provided by the 'Analyzer'. For this purpose, the forming limits of the different fracture criteria are written as a function of the three following functions related to the accumulation of ductile damage by tension (7), in-plane shear (8), and out-of-plane shear (9).

$$\bar{\varepsilon} = \frac{D_{\mathrm{crit}}}{\eta} \tag{7}$$

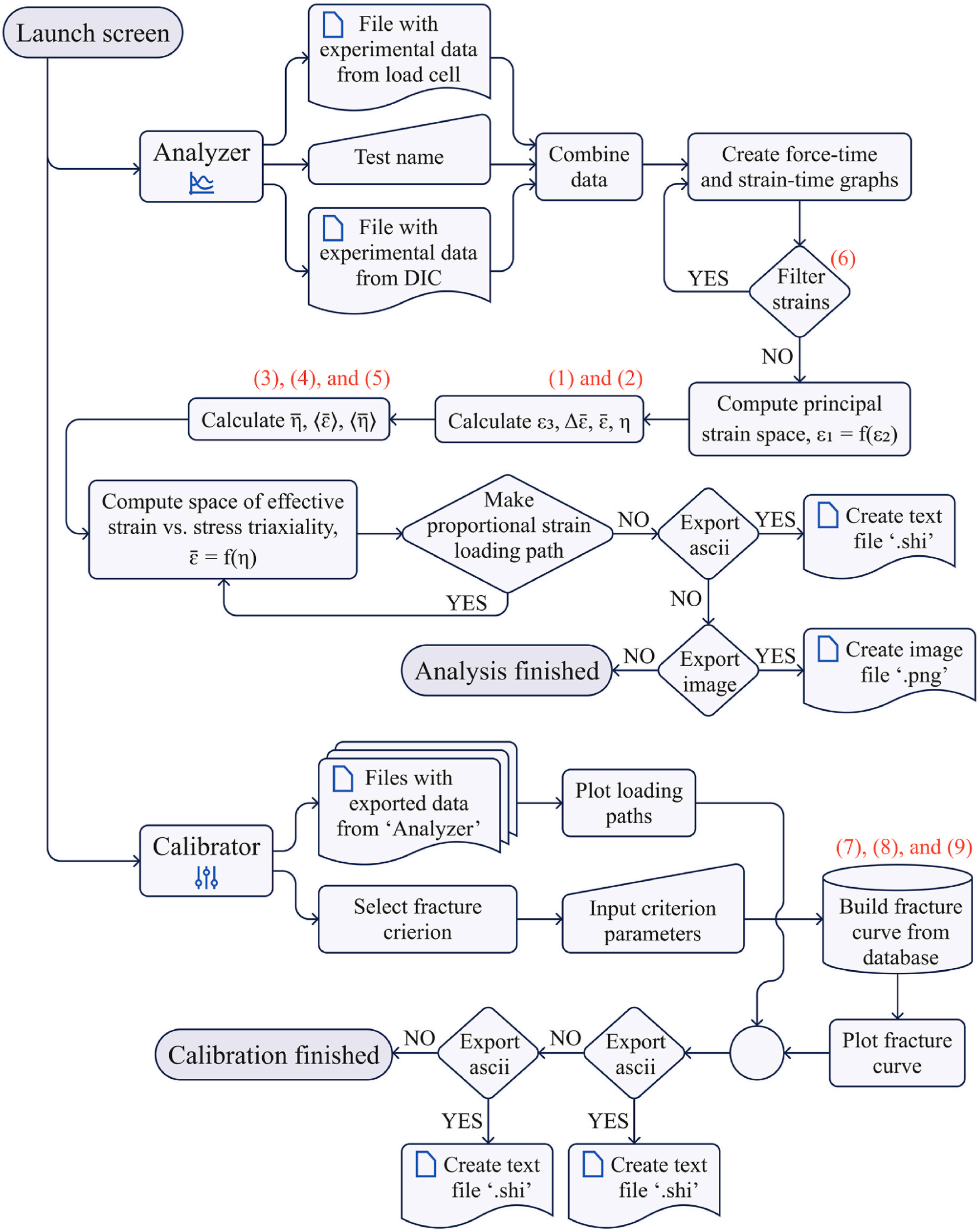

Fig. 5. The software user flow with the equation numbers in brackets.

$$\bar{\varepsilon} = \frac{D_{\text{crit}}}{\tau_{12}/\bar{\sigma}} \tag{8}$$

$$\bar{\varepsilon} = \frac{D_{\text{crit}}}{\tau_{ti}/\bar{\sigma}}, \text{ with } i = 1, 2 \tag{9}$$

In the above equations τ_{12} is the in-plane shear stress and τ_{ti} is the maximum out-of-plane (or through-thickness) shear stress.

The normalized Cockcroft-Latham ductile fracture criterion, for example, can be written in terms of the through-thickness shear stress (Martins et al., 2014), as follows,

$$D^{\text{NCL}}_{\text{crit}} = \int_0^{\bar{\varepsilon}_f} \frac{\sigma_1}{\bar{\sigma}} d\bar{\varepsilon} = \int_0^{\bar{\varepsilon}_f} 2\frac{\tau_{ti}}{\bar{\sigma}} d\bar{\varepsilon} \tag{10}$$

Now, considering equations (9) and (10), the forming limit curve corresponding to this criterion can be written as a function of the stress triaxiality η, inverse slope of the strain loading path β, and anisotropy factor r (refer to Appendix A). The pseudo code for implementation of

Experimental Strain Loading Path Analyzer

Upload RAW or CSV file: 6082-O-Tens-A_RawData.csv (88 kB)

Upload Text file: 6082-O-Tens-A_DICExport.txt (113 kB)

Test name: AA6082-O_tensile_A

Moving average filter parameter: 145

Strain Loading Paths

Slope at cracking (°): 287

Time at fracture	184.6 s
ε_1 at fracture	0.629
ε_2 at fracture	-0.306
ε_3 at fracture	-0.323
$\Delta\varepsilon_e$ at fracture	5.13E-4
ε_e at fracture	0.633
η at fracture	0.455
η_{av} at fracture	0.341
$\langle\varepsilon_e\rangle$ at fracture	0.632
$\langle\eta_{av}\rangle$ at fracture	0.455

Steps interval for slope calculations: 1

☐ Make proportional loading path for the first step

Fracture Criteria Calibrator

● Shiro ○ i-form

Normalized Cockcroft-L...

r = 1

D = 0.64

$(\varepsilon_e)_{max}$ = 1

☑ Use average triaxiality

☑ Exclude values at which damage does not accumulate

Fig. 6. Screenshots of the (a) analyzer and (b) calibrator user interfaces for a rod tension test.

the normalized Cockcroft-Latham ductile fracture criterion is given below, in which appropriate reference to the previous equations are included in brackets:

```
SET TriaxialityCount to -1.0/3.0
WHILE TriaxialityCount is less than 2.0/3.0
    IF TriaxialityCount is greater than CriterionAsymptote THEN
        CALCULATE Beta (equation 2)
        CALCULATE WeightingFunction
        CALCULATE EffectiveStrain (equations 7 through 10)
    END IF
    ADD Increment to TriaxialityCount
END WHILE
```

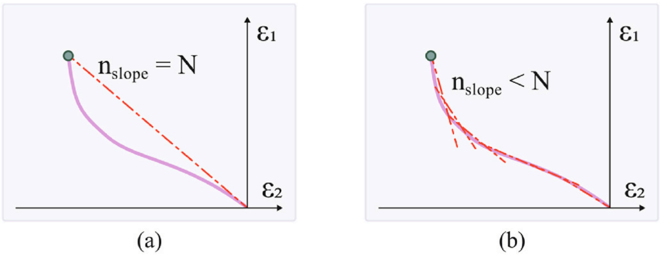

Fig. 7. Selecting a step interval n_{slope} (a) equal to and (b) smaller than the total number of experimental points N for calculating the inverse slope of the strain loading path $\beta = d\varepsilon_2/d\varepsilon_1$.

Pseudo code for implementation of the normalized Cockcroft-Latham ductile fracture criterion.

The 'Calibrator' interface allows determining the fracture forming limit curves corresponding to different ductile fracture criteria directly from the raw experimental data of the non-linear strain loading paths. This minimizes the risk of getting wrong results due to variations in the accumulation of damage for different stress states and can be seen as an alternative to the use of inverse calibration procedures based on finite element digital twins (Sun et al., 2022).

4. Results and discussion

4.1. Loading paths

Fig. 8a shows the experimental force-time evolution $F(t)$ obtained from the load cell and the in-plane strain-time evolutions $(\varepsilon_1, \varepsilon_2) = f(t)$ obtained from the DIC system for the double-action radial extrusion tests, as supplied to the 'Analyzer' interface by the authors. The time at the instant of fracture t_f was automatically determined by the software by searching for a sudden drop in the force-time evolution $F(t)$.

Combination of the in-plane strain-time evolutions $(\varepsilon_1, \varepsilon_2) = f(t)$ to obtain the strain loading paths in principal strain space $\varepsilon_1 = f(\varepsilon_2)$ was

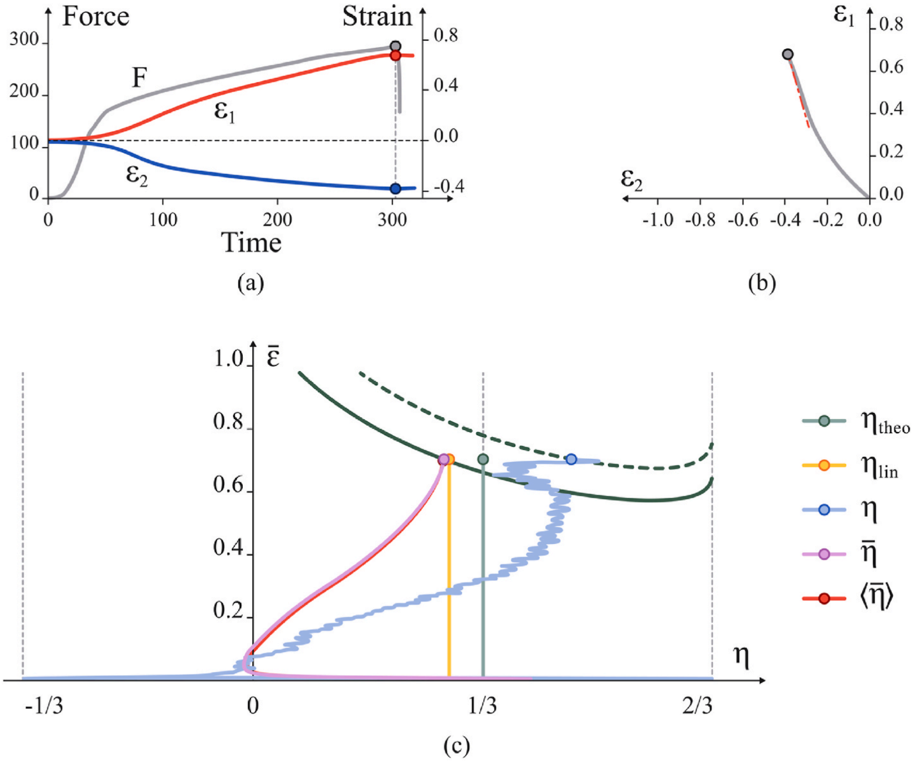

Fig. 8. Utilization of the software to (a) analyze raw experimental data from the load cell and DIC and determine the instant of fracture, (b) obtain the strain loading path in principal strain space and transform results into (c) the effective strain vs. stress triaxiality space under different assumptions and stress triaxiality measures.

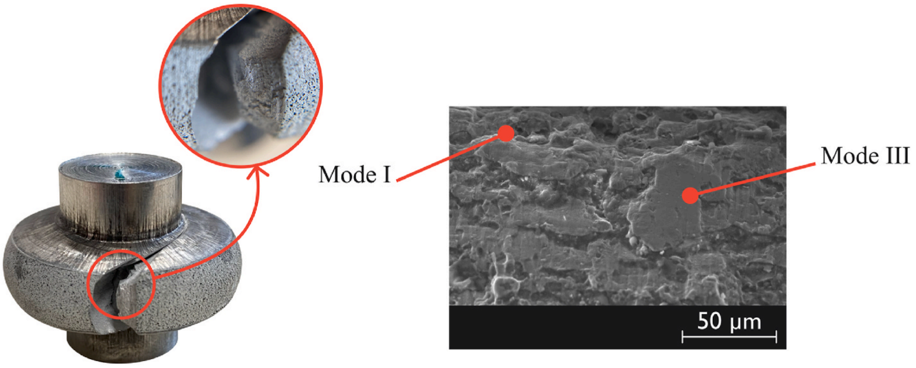

Fig. 9. Photograph of a test specimen at fracture with SEM image of the cracked surfaces.

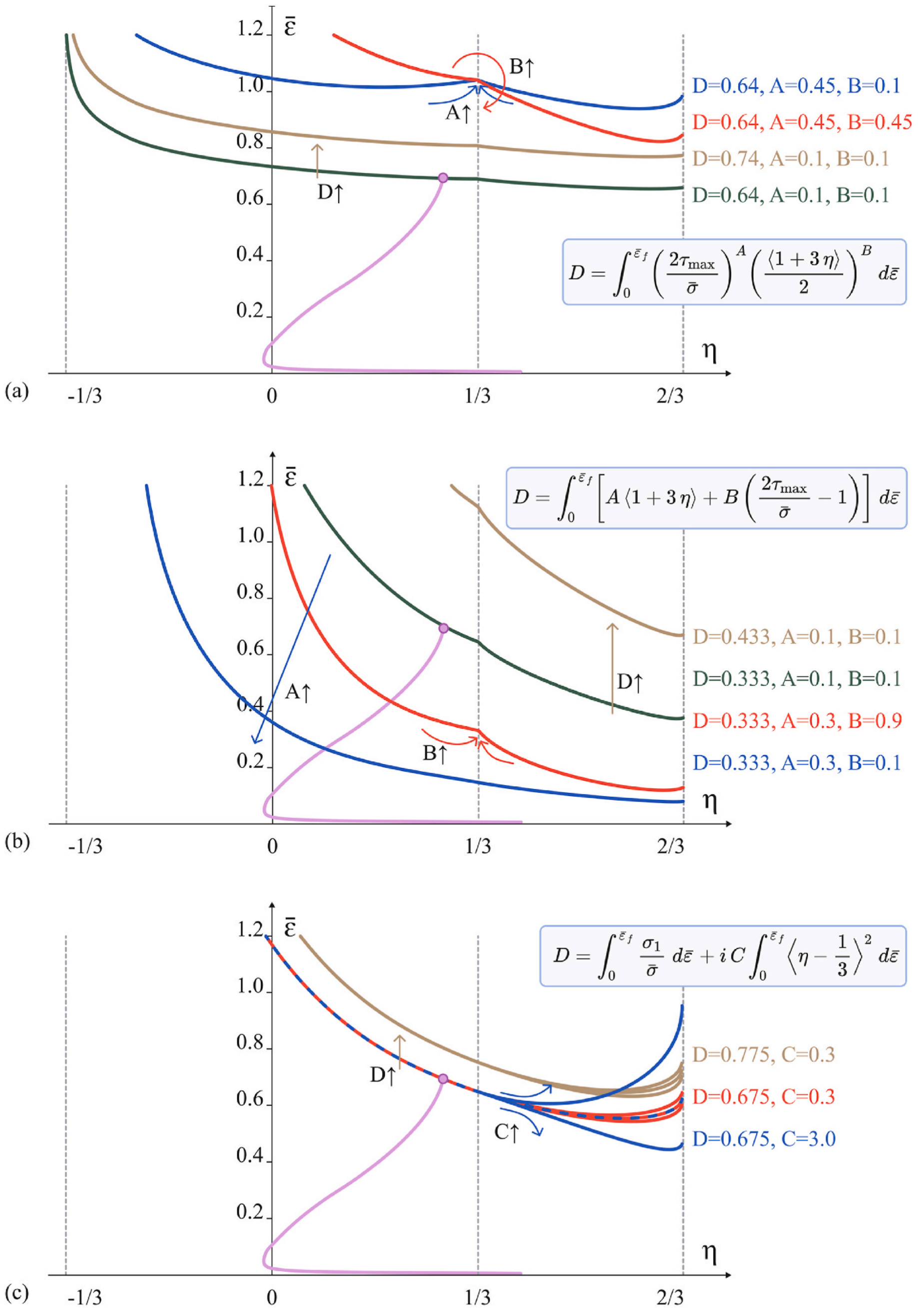

Fig. 10. Variation of the fracture forming limits by changing the values of the main parameters of three different ductile fracture criteria: (a) Lou et al. (2012), (b) Isik (2018) and (c) Sampaio et al. (2023b).

also automatically performed by the software. The result is shown in Fig. 8b and allows concluding about the non-linear characteristics of the strain loading path due to the existence of two different forming stages: (i) upsetting and (ii) radial extrusion.

In the earliest stage, material is upset to fill out the containers and to be progressively deformed into the free gap heigh between the containers. This leads to a sharp increase in the required force (Fig. 8a) and to an initial shear strain loading path at the outer surface of the specimens (Fig. 8b). In the radial extrusion stage, the strain loading path is progressively bent into pure tension (Fig. 8b), as the flange starts to emerge through the free gap height. The required force continues to grow but at a lower rate, as shown in Fig. 8a.

The last calculation of the 'Analyzer' interface consists of the transformation of the strain loading path into the effective strain vs. stress triaxiality space $\bar{\varepsilon} = f(\eta)$ through the utilization of different assumptions and stress triaxiality measures. The result is shown in Fig. 8c, where the material fracture forming limit corresponding to the critical damage D_{crit} is given by the dark green curve that had been previously determined by the authors (Sampaio et al., 2023a).

As seen, the assumption of a linear strain loading path (refer to the orange line) from beginning to the onset of cracking $(\varepsilon_{1f}, \varepsilon_{2f})$ provide a conjugate pair $(\eta_f, \bar{\varepsilon}_f)$ of stress triaxiality and effective strain at fracture in close agreement with the fracture forming limit. Full characterization of the non-linear strain loading path requires accountability of the multiple in-plane strains $(\varepsilon_{1i}, \varepsilon_{2i})$ up to fracture and conversion into the effective strain vs. stress triaxiality space $\bar{\varepsilon} = f(\eta)$ by means of an adequate stress triaxiality measure. In fact, while the utilization of instantaneous η_i stress triaxiality leads to a conjugate pair at fracture that is positioned significantly away from the fracture forming limit, the utilization of weighted average stress triaxiality $\bar{\eta}$ and weighted average stress triaxiality at which damage accumulates $\langle\overline{\eta}\rangle$, provides conjugate pairs at fracture that are on top of the fracture forming limit (Fig. 8c).

The reason why $\langle\overline{\eta}\rangle \cong \overline{\eta}$ is because the fracture strains associated with the two aforementioned stress triaxiality measures are similar $\langle\overline{\varepsilon}\rangle \cong \overline{\varepsilon}$ due to the inexistence of negative stress states at the outer flange surface during double-action radial extrusion.

The differences between the experimental loading paths obtained from the utilization of instantaneous η_i and weighted average $\overline{\eta}$ stress triaxiality measures are compatible with those obtained by Suntaxi et al. (2021) for the finite element modelling of tube expansion by single point incremental forming. The inexistence of negative stress states at the outer flange surface during double-action radial extrusion explain the reason why $\overline{\eta} = \langle\overline{\eta}\rangle$.

The loading path corresponding to pure tension is included in Fig. 8c (refer to the light green line), and the difference to the other paths is attributed to the fact that the outer flange does not experience plastic deformation under pure tension.

The conjugate pair $(\eta_f, \overline{\varepsilon}_f)$ at fracture, calculated from weighted average stress triaxiality $\overline{\eta}$ values, is located slightly to the left of pure tension $\eta = 1/3$. This result is consistent with the fact that cracks do not run radially, as expected in a pure tension state of stress (Fig. 9). In fact, the morphology of the cracked surfaces obtained from scanning electron microscopy (SEM) discloses a mixed opening mode characterized by some patches of globular dimple structures (typical of mode I) among smooth parabolic dimple-based structures (typical of mode III).

4.2. *Calibration, education, and training*

The previous section analyzed how different assumptions and stress triaxiality measures influence the transformation of the strain loading paths up to fracture into the effective strain vs. stress triaxiality space $\overline{\varepsilon} = f(\eta)$. Once these loading paths are available for a wide range of stress states, they can all be uploaded in the 'Calibrator' interface (Fig. 5) to calibrate the different ductile fracture criteria available in the software. This is done by changing the different parameters of the ductile fracture criteria so that the fracture forming limits match the conjugate pairs $(\eta_f, \overline{\varepsilon}_f)$ of the different stress triaxiality and effective strain values at fracture.

Fig. 10 illustrates how the fracture forming limit corresponding to three different ductile fracture criteria can be handled and analyzed in the effective strain vs. stress triaxiality space $\overline{\varepsilon} = f(\eta)$ by changing the values of its main parameters.

The examples included in Fig. 10 illustrate the application of the software for educational purposes due to the easiness of plotting specific fracture criteria and analyzing the sensitivity to their main parameters in the effective strain vs. stress triaxiality space $\overline{\varepsilon} = f(\eta)$. The modular construction of the 'Calibrator' interface also allows to include other criteria than those originally available in the software.

The interface also helps understand how each parameter relates to the shearing and tension effects that govern void growth mechanisms, and how they affect the overall profile of the fracture forming limits. For all these reasons, it can be considered an effective tool for both research and education in material formability.

5. Conclusions

Accountability of stress triaxiality by means of new measures that consider the differences in the accumulation of damage between different stress states proved to be more effective and compatible with the fracture forming limits and the morphology of fracture surfaces than instantaneous stress triaxiality.

Utilization of the different stress triaxiality measures for processing and combining raw experimental data from load cells and DIC systems led to the development of a software that automatically converts arbitrary non-linear loading paths from principal strain space into the effective strain vs. stress triaxiality space.

Results for double-action radial extrusion tests confirm the applicability of the software for handling and treating experimental data for both scientific and educational purposes. The calibration features of the software allow its broader use for helping students to diminish the gap between ductile fracture criteria, the experimental calibration of the fracture forming limits and their use in practical metal forming applications.

Declaration of competing interest

The authors declare that they have no known competing financial interests or personal relationships that could have appeared to influence the work reported in this paper.

Data availability

Data will be made available on request.

Acknowledgments

The authors would like to acknowledge the support provided by Fundação para a Ciência e a Tecnologia of Portugal and IDMEC under LAETA- UIDB/50022/2020 and PTDC/EME-EME/0949/2020. Rui Sampaio would also like to acknowledge the support under the PhD Studentship 2022.12351.BD. Additional acknowledgements are given to Collletttivo for the design of the Apfel Grotezk typeface and to Alexandra Korolkova and Vitaly Kuzmin for the design of the Golos Text typeface utilized in the software.

Appendix B. Supplementary data

Supplementary data to this article can be found online at https://doi.org/10.1016/j.aime.2023.100127.

Appendix A

To plot fracture criteria in the space of stress triaxiality vs. effective strain one needs to write the weighting functions as functions of stress triaxiality. However, it was demonstrated by Sampaio et al. (2022) that the slope of the loading path β can also be written as a function of stress triaxiality. If a similar approach is taken into consideration, but now accounting for anisotropy, the resulting expression is the following,

$$\beta = \frac{-2\left(\frac{9\eta^2 r}{(1+r)} - (1+2r)\right) - 6\eta\sqrt{-\left(\frac{9\eta^2}{(1+r)^2} - \frac{2}{(1+r)}\right)(1+2r)}}{2(9\eta^2 - (1+2r))} \tag{A.1}$$

where r is the anisotropy factor according to Hill's (1948) yield criterion.

This means that one can write the weighting functions for the various fracture criteria as functions of both η and β (and, of course r, if anisotropy is considered).

From Martins et al. (2014) one can write the following expression for the normalized major principal stress component $\sigma_1/\overline{\sigma}$ based on stress triaxiality η and slope of the loading path β,

$$\frac{\sigma_1}{\overline{\sigma}}=\frac{3[(1+r)+r\beta]}{(1+2r)(1+\beta)}\eta \tag{A.2}$$

From Sampaio et al. (2023b), the normalized maximum shear stress may be written as follows,

$$\frac{\tau_{\max}}{\overline{\sigma}}=\begin{cases}\dfrac{\tau_{12}}{\overline{\sigma}}, -\dfrac{1}{3}\leq\eta<\dfrac{1}{3}\\ \dfrac{\tau_{ti}}{\overline{\sigma}}, \eta<-\dfrac{1}{3}\vee\eta\geq\dfrac{1}{3}\end{cases} \tag{A.3}$$

where $\tau_{12}/\overline{\sigma}$ is the normalized in-plane shear stress and $\tau_{ti}/\overline{\sigma}$ is the normalized through-thickness (or out-of-plane) shear stress.

From Martins et al. (2014), one can write both as,

$$\frac{\tau_{ti}}{\overline{\sigma}}=\frac{1}{2}\frac{\sigma_1}{\overline{\sigma}}=\frac{3}{2}\frac{[(1+r)+r\beta]}{(1+2r)(1+\beta)}\eta \tag{A.4}$$

$$\frac{\tau_{12}}{\overline{\sigma}}=\frac{1-\alpha}{2}\frac{\sigma_1}{\overline{\sigma}} \tag{A.5}$$

where α is the ratio between the intermediate and major principal stress components,

$$\alpha=\frac{\sigma_2}{\sigma_1}=\frac{(1+r)\beta+r}{(1+r)+r\beta} \tag{A.6}$$

Equations (A.2) and (A.6) can finally be combined to write the normalized in-plane shear stress as a function of the stress triaxiality η, the slope of the strain loading path β and the anisotropy factor r, as follows,

$$\frac{\tau_{12}}{\overline{\sigma}}=\frac{3}{2}\frac{(1-\beta)}{(1+2r)(1+\beta)}\eta \tag{A.7}$$

References

Ayada, M., Higashino, T., Mori, K., 1987. Central bursting in extrusion of inhomogeneous materials. In: Proceedings of the Proceedings of the Second International Conference on Technology of Plasticity, vol. I, pp. 553–558 (Stuttgart, Germany).

Bai, Y., Wierzbicki, T., 2008. A new model of metal plasticity and fracture withpressure and Lode dependence. Int. J. Plast. 24, 1071–1096. https://doi.org/10.1016/j.ijplas.2007.09.004.

Cockcroft, M.G., Latham, D.J., 1968. Ductility and the workability of metals. J. Inst. Met. 96, 33–39.

Goodwin, G.M., 1968. Application of strain analysis to sheet metal forming problems in the press shop. In: 1968 Automotive Engineering Congress and Exposition, SAE International, Paper 680093, Detroit, MI, USA. https://doi.org/10.4271/680093.

Hancock, J.W., Mackenzie, A.C., 1976. On the mechanisms of ductile failure in high-strength steels subjected to multi-axial stress-states. J. Mech. Phys. Solid. 24, 147–169. https://doi.org/10.1016/0022-5096(76)90024-7.

Hill, R., 1948. A theory of the yielding and plastic flow of anisotropic metals. P. Roy. Soc. Lond. A Mat. 193, 281–297. https://doi.org/10.1098/rspa.1948.0045.

Ishigaki, H., 1978. Deformation analysis of large sized panels in the press shop. In: Koistinen, D.P., Wang, N.M. (Eds.), Mechanics of Sheet Metal Forming. Plenum Press, New York, NY, USA, pp. 315–339. https://doi.org/10.1007/978-1-4613-2880-3_13.

Isik, K., Silva, M.B., Tekkaya, A.E., Martins, P.A.F., 2014. Formability limits by fracture in sheet metal forming. J. Mater. Process. Technol. 214, 1557–1565. https://doi.org/10.1016/j.jmatprotec.2014.02.026.

Isik, K., 2018. Modelling and Characterization of Damage and Fracture in Sheet-Bulk Metal Forming. PhD Dissertation, Technischen Universität Dortmund, Dortmund, Germany.

Keeler, S.P., 1965. Determination of forming limits in automotive stampings. SAE Trans. 74, 1–9.

Kuhn, H.A., Lee, P.W., Ertuk, T., 1973. A fracture criterion for cold forming. J. Eng. Mater. Technol. 95, 213–218. https://doi.org/10.1115/1.3443155.

Lode, W., 1926. Versuche über den Einfluß der mittleren Hauptspannung auf das Fließen der Metalle Eisen, Kupfer und Nickel. Z. Phys. 36, 913–939. https://doi.org/10.1007/BF01400222.

Lou, Y., Huh, H., Lim, S., Pack, K., 2012. New ductile fracture criterion for prediction of fracture forming limit diagrams of sheet metals. Int. J. Solid Struct. 49, 3605–3615. https://doi.org/10.1016/j.ijsolstr.2012.02.016.

Magrinho, J.P., Silva, M.B., Alves, L.M., Atkins, A.G., Martins, P.A.F., 2018. New methodology for the characterization of failure by fracture in bulk forming. J. Strain Anal. Eng. 53, 242–247. https://doi.org/10.1177/0309324718758842.

Martins, P.A.F., Bay, N., Tekkaya, A.E., Atkins, A.G., 2014. Characterization of fracture loci in metal forming. Int. J. Mech. Sci. 83, 112–123. https://doi.org/10.1016/j.ijmecsci.2014.04.003.

McClintock, F.A., 1968. A criterion for ductile fracture by the growth of holes. J. Appl. Mech. 35, 363–371. https://doi.org/10.1115/1.3601204.

Microsoft, 2023. What is .NET MAUI? https://docs.microsoft.com/en-us/dotnet/maui/what-is-maui/. (Accessed 21 March 2023).

Oh, S.-I., Chen, C.C., Kobayashi, S., 1979. Ductile fracture in axisymmetric extrusion and drawing—Part 2: workability in extrusion and drawing. J. Eng. Ind. 101, 36–44. https://doi.org/10.1115/1.3439471.

Oyane, M., 1972. Criteria of ductile fracture strain. Bull. JSME 15, 1507–1513. https://doi.org/10.1299/jsme1958.15.1507.

Paul, S.K., 2021. Controlling factors of forming limit curve: a review. Adv. Ind. Manuf. Eng. 2, 100033 https://doi.org/10.1016/j.aime.2021.100033.

Peters, W.H., Ranson, W.F., 1982. Digital imaging techniques in experimental stress analysis. Opt. Eng. 21, 427–431. https://doi.org/10.1117/12.7972925.

Rice, J.R., Tracey, D.M., 1969. On the ductile enlargement of voids in triaxial stress fields. J. Mech. Phys. Solid. 17, 201–217. https://doi.org/10.1016/0022-5096(69)90033-7.

Sampaio, R.F.V., Pragana, J.P.M., Bragança, I.M.F., Silva, C.M.A., Martins, P.A.F., 2022. Revisiting the fracture forming limits of bulk forming under biaxial tension. Int. J. Damage Mech. 31, 882–900. https://doi.org/10.1177/10567895211072580.

Sampaio, R.F.V., Pragana, J.P.M., Bragança, I.M.F., Silva, C.M.A., Nielsen, C.V., Martins, P.A.F., 2023a. Characterization of the fracture forming limits by radial extrusion. J. Manuf. Mater. Process. 7 https://doi.org/10.3390/jmmp7030107.

Sampaio, R.F.V., Pragana, J.P.M., Bragança, I.M.F., Silva, C.M.A., Martins, P.A.F., 2023b. A complete characterization of fracture forming limits in bulk forming: an upset geometry sequence. J. Strain. Anal. Eng. https://doi.org/10.1177/03093247231187015 (accepted for publication).

Silva, C.M.A., Sampaio, R.F.V., Pragana, J.P.M., Bragança, I.M.F., Martins, P.A.F., 2023. An upset geometry sequence for determining the formability limits in bulk forming. CIRP Ann. https://doi.org/10.1016/j.cirp.2023.04.009.

Smith, S.W., 2003. Moving average filters. In: Digital Signal Processing – A Practical Guide for Engineers and Scientists. Newnes, Boston, MA, USA, pp. 277–284. https://doi.org/10.1016/B978-0-7506-7444-7/50052-2.

Sun, L., Cai, Z., Gao, J., Wang, M., Li, L., 2022. Calibration of ductile fracture criterion with optimal experiment design and prediction on forming limit for aluminum alloy sheet. Met. Mater. Int. 28, 848–861. https://doi.org/10.1007/s12540-021-00970-3.

Suntaxi, C., Centeno, G., Silva, M.B., Vallellano, C., Martins, P.A.F., 2021. Tube expansion by single point incremental forming: an experimental and numerical investigation. Metals 11, 1481. https://doi.org/10.3390/met11091481.

Tai, W.H., Yang, B.X., 1987. A new damage mechanics criterion for ductile fracture. Eng. Fract. Mech. 27, 371–378. https://doi.org/10.1016/0013-7944(87)90174-3.